Journal of Materials Chemistry A

Accepted Manuscript

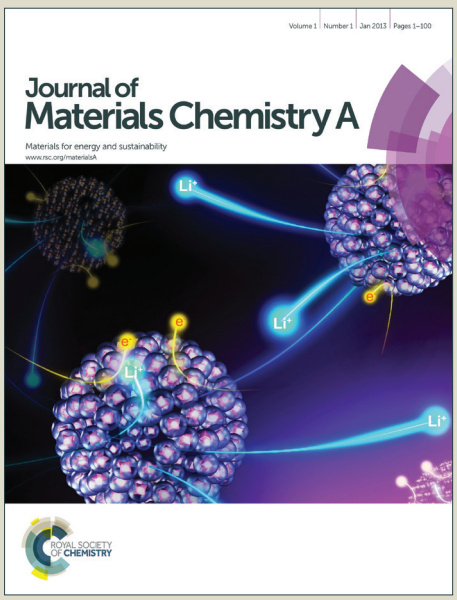

ROYAL SOCIETY OF CHEMISTRY

www.rsc.org/materialsA

Control of Chemical State of Cerium in Doped Anatase TiO_2 by Solvothermal Synthesis and its Application in Photocatalytic Water Reduction

Juliana Fonseca de Lima,[1,2] Mohammad Hilni Harunsani,[1‡] David James Martin,[3,4] Dan Kong,[3] Peter W. Dunne,[1] Diego Gianolio,[5] Reza J. Kashtiban,[6] Jeremy Sloan,[6] Osvaldo Antonio Serra,[2] Junwang Tang[3*] and Richard I. Walton[1*]

1. Department of Chemistry, University of Warwick, Coventry, CV4 7AL, U.K.

2. Department of Chemistry, FFCLRP, USP, Av. Bandeirantes 3900, CEP 14040-901 Ribeirão Preto, SP, Brazil

3. Department of Chemical Engineering, University College London, London WC1E 7JE, U.K.

4. Department of Chemistry, University College London, London, WC1H 0AJ, U.K.

5. Diamond Light Source Ltd., Harwell Science and Innovation Campus, Didcot OX11 0DE, U.K.

6. Department of Physics, University of Warwick, Coventry, CV4 7AL, U.K.

‡ Present address: Universiti Brunei Darussalam, Faculty of Science, Jln. Tungku Link, Gadong, BE1410, Brunei Darussalam

Table of contents entry

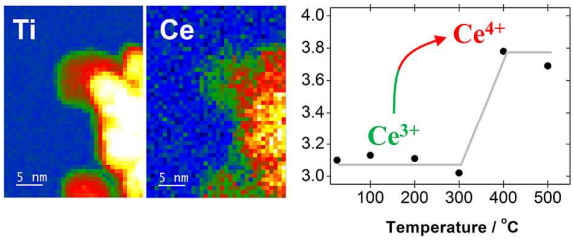

Solvothermal synthesis in ethanol yields nanocrystalline Ce^{3+}-doped TiO_2 that shows high activity for photocatalytic water reduction; upon annealing oxidation to Ce^{4+} occurs with loss of activity.

Abstract

Solvothermal synthesis at 240 °C in ethanol from titanium(IV) isopropoxide and cerium(III) nitrate hexahydrate produces nanocrystalline powders of anatase-structured TiO_2. At low Ce content (0.5 mol % Ti replaced by Ce) the materials contain mixtures of Ce^{3+} and Ce^{4+}, seen from Ce L_{III}-edge X-ray absorption near-edge structure (XANES) spectroscopy, which are well dispersed in the anatase structure as evidenced from nanometre-scale electron energy loss spectroscopy maps and powder X-ray diffraction (XRD), respectively. The addition of lactic acid to the solvothermal reaction produces less crystalline samples, proved by powder XRD and Raman spectroscopy, with higher surface areas from nitrogen adsorption, and that contain a higher proportion of Ce^{3+}. This leads to material with high activity for photocatalytic hydrogen production from water under UV irradiation in the presence of sacrificial methanol and Pt catalyst. Further *in situ* XANES experiments at the Ce L_{III}-edge recorded on heating the materials in air above 300 °C shows that oxidation to Ce^{4+} occurs. This process, typical of the conditions usually used in the synthesis of Ce-doped titania materials, yields materials with lower photocatalytic activity.

Introduction

The photocatalytic properties of titanium dioxide polymorphs are well documented and have established applications in areas such as solar energy conversion devices and photochemical pollutant removal.[1, 2] Recently there has been renewed interest in photocatalytic splitting of water, in particular for the sustainable production of hydrogen as a clean energy supply.[3] One tactic in optimising the photochemical activity of titanium oxides is the introduction of dopant elements, which may allow tuning of the electronic properties, and these may either be metal ions, replacing some of the Ti,[4] or anions, where oxide is partially replaced by some other anionic entity.[5] Hand-in-hand with such chemical manipulation, control of crystal morphology is also an important way to tune properties of titania materials and structure on the nanoscale may be beneficial for optimising photocatalysis properties;[6] particular focus has been on faceted crystals that may present reactive crystal faces,[7] and also nano-scale interfaces between two or more TiO_2 polymorphs.[8] In this field, a particularly striking example was recently provided by the report of 'black TiO_2' where hydrogenation of pre-made nanocrystalline anatase TiO_2 introduces a disordered surface layer of hydrogen-doped titanium oxide, which may also be highly oxygen deficient.[9, 10] Black TiO_2 shows visible light absorption, not shown by pure TiO_2, as well as UV absorption, and this contributes to its high activity in photocatalytic water splitting, although it is not believed to be solely responsible, since structural disorder also play a role in its high activity.[11]

Herein we describe a straightforward synthesis approach to the formation of Ce-containing TiO_2 that involves direct crystallisation under solvothermal conditions from an ethanolic solution of metal salts, without any post-synthesis annealing needed to induce crystallinity. It is well known that cerium is found in two common oxidation states in oxide, +3 and +4, and cerium oxide itself is renowned for its redox catalytic properties, involving reversible switching between these oxidation states in the solid state via oxygen loss.[12] Both Ce^{3+} and Ce^{4+} have considerably larger ionic radii than Ti^{4+} in common coordination environments,[13] and are never found in octahedral coordination in any bulk, stoichiometric oxides; therefore the extent of Ce doping into TiO_2 polymorphs (all of

which contain octahedrally coordinated Ti) is expected to be limited. Although there are some previous reports that propose either Ce^{3+} or Ce^{4+} are included in TiO_2,[14, 15, 16, 17-19] few of these studies measured full characterisation data to enable the location of cerium, its valence state, and the charge-balancing mechanism to be determined. Indeed, almost all of the previous synthesis routes to Ce-TiO_2 materials have used an annealing in air of typically 500 °C to crystallise the materials, which will undoubtedly form Ce^{4+}-rich materials and can also result in the formation of phase-separated mixtures of binary oxides.[18] Such materials have largely been studied for photocatalytic organic decomposition, rather than the more challenging water splitting reaction, and it is an open question as to the optimum concentration and distribution of Ce oxidation state for catalysis. In other related works, mixed CeO_x-TiO_2 particles have been prepared purposely for photocatalysis; for example Luo *et al.* recently deposited defective CeO_2 nanoparticles on the surface of pre-made anatase TiO_2 to introduce photocatalytically active interfaces.[20] Our synthesis approach is to crystallise atomically mixed-metal oxide materials directly from solution and to study them in their 'as-made' form. By this method we can maintain a large amount of Ce^{3+}, also aided by the inclusion of lactic acid in the crystallisation, as we prove using XANES spectroscopy. This yields materials with high photocatalytic water-splitting activity for production of hydrogen in the presence of sacrificial methanol and Pt catalyst.

Results and Discussion

1. Structural Characterisation

Powder XRD shows all samples possess the average anatase structure, with no diffraction features due to one of the other polymorphs of TiO_2, Figure 1. The broadened profile is consistent with the small particle size as seen by electron microscopy (see below) while full profile refinements of the powder patterns allows the behaviour of lattice parameters with Ce concentration to be determined, Figure 2. The refined lattice parameters fall within the range of those reported previously for anatase TiO_2 prepared by solution synthesis, where the literature shows that the unit cell dimensions

can be highly dependent on crystal size and may also be sensitive to defects (see Supporting Information). Thus while the unit cell volume of highly crystalline anatase is 136.26 $Å^3$ at room temperature (JCPDS 84-1285, taken from Burdett *et al.*[21]), for anatase prepared as small particles from solution, a range of unit cell volumes have been reported, from 133 to 137 $Å^3$ (see Supporting Information). For nanocrystalline anatase TiO_2 it has been reported that there is a dependence of lattice parameters on crystallite size, especially for crystallites of less than 40 nm in dimension, with an increase of *a*, decrease of *c* and net unit cell volume increase with diminishing crystallite size.[22]

Using our synthetic method, materials with a Ti:Ce ratio of up to 0.90:0.10 (10%Ce-TiO_2) can be formed, before the appearance of characteristic Bragg peaks of fluorite CeO_2 are seen in the diffraction pattern at 15% Ce. At low Ce concentration (up to 1% Ce) the tetragonal lattice parameters of TiO_2 show a marked expansion relative to crystalline anatase, which is followed by a general levelling off with further addition of Ce to 10%. This may suggest a maximum amount of Ce is added to the anatase, but it is important to note that even for the highest Ce content where the samples are most crystalline (see Figure 1) the *c* parameter is somewhat different than for bulk anatase, suggesting that at least some Ce may be included in the lattice. A similar effect has been reported by others for lanthanide-doped TiO_2.[19] After treating the as-made materials by holding in air at 400 ^oC for 4 hours, the powder XRD shows little evidence of Bragg peak sharpening, but the lattice parameters show a less pronounced variation with Ce content (Supporting Information). Scherrer analysis of the broadened diffraction profile allows crystallite sizes to be estimated, as shown in Table 1. Table 1 also contains the results of surface areas determined by BET analysis (see Supporting Information for isotherms), and confirms that materials prepared with the smallest Ce concentrations have the smallest crystallites and the highest surface areas. As the Ce concentration is increased the materials become more crystalline with lower surfaces areas. Furthermore, the presence of lactic acid in synthesis always produces materials with higher surface area and smaller crystal domain size. The smaller crystallite size of the lowest Ce containing materials is likely to be a contributing factor to their larger unit cell volumes.

High temperature powder XRD shows that transformation of the anatase materials to the rutile polymorph at temperatures above 800 °C is inhibited compared to pure TiO_2 (see Supporting Information for temperature-resolved powder X-ray diffraction), which has previously been noted in other mixed cerium-titanium oxides.[15] This suggests an intimate mixing of cerium species with the anatase TiO_2. Taken together, all the powder XRD results suggest an atomic-scale interaction between the cerium and TiO_2.

Scanning transmission electron microscopy was used to image the crystallites and to examine the distribution of Ce and Ti in the samples using electron energy loss spectroscopy (EELS) mapping (Figure 3). For the 1%Ce-TiO_2 material crystallites of less than 10 nm are seen, while slightly larger primary particles are seen for the 10%Ce-TiO_2 sample. The element-selective EELS mapping clearly shows that Ce is present in all regions of samples studied, in the same regions as the Ti (see Supporting Information for further images), and there is no evidence from this technique of Ce segregation, for example on the surface of the particles. The bulk elemental ratios of the metals in the solids determined by ICP analysis are very close to the values used in synthesis, showing that all the intended metals used in the solution synthesis are included in the solid products (Supporting Information).

Raman spectroscopy, Figure 4, shows distinct trends in peak positions and peak broadening with Ce content. All bands can be assigned as arising from the tetragonal anatase structure by reference to the literature[23] and there is no evidence for cubic CeO_2 in any of the samples, or indeed other polymorphs of TiO_2. It is well-documented that any shift in the position and the width of the $E_g(1)$ band of anatase is due to a combination of small particle size and the presence of defects (or dopants), and can be thus used as a diagnostic of nanocrystalline structure.[24] For the samples prepared in the presence of lactic acid the peak position is always shifted to higher wavenumber than those made without lactic acid, although within each set (with and without lactic acid), there is little trend in peak position with cerium content. This is consistent with the smaller crystallite size of the materials prepared in lactic acid. The $E_g(1)$ band is also always broader for the materials

made in lactic acid, and furthermore shows a positive dependence with increasing Ce content only when lactic acid is included in the synthesis, with a notable broadening as more Ce is added. This is rather counterintuitive given the increasing particle size seen by XRD and TEM with increased Ce content, but would be consistent with the lactic acid producing more defective anatase structure on the local scale and also that perhaps that the presence of lactic acid has some cooperative effect with cerium, for example, allowing a greater incorporation into the anatase lattice. Similar local disorder effects have been seen before: for example co-doped Ce,Nd samples of anatase have been reported to show similar broadening of the $E_g(1)$ band.[25]

IR spectroscopy was used to examine the possibility of the presence of organic species that might derive from the lactic acid or titanium isopropoxide used in synthesis, Figure 5. Although extra bands are seen in the spectra of all samples in the organic fingerprint region of the spectra, these cannot be assigned as due to lactate or isopropoxide moieties. Nevertheless, the spectra clearly show the presence of organic species, which may be either lattice incorporated, or surface bound. Given the relatively large surface area the latter possibility is a distinct possibility. Thermogravimetric analysis shows larger percentage mass losses for the samples that contain cerium (despite the higher formula weight of the oxide), suggesting the inclusion of more organic as a function of cerium concentration (Supporting Information).

The oxidation state of Ce was examined using Ce L_{III}-edge X-ray absorption near edge spectroscopy (XANES), which uses high energy incident X-rays to excite core-level electrons and probes bulk, average local environment of all cerium. The Ce L_{III}-edge is proven to be sensitive to oxidation state of Ce in oxide materials, where for the cerium (III) oxides a single 'white line' is seen, corresponding to the electronic transition $2p_{3/2} \rightarrow (4f^1)5d$, and for cerium (IV) oxides a double feature comprising of $2p_{3/2} \rightarrow (4fL)5d$ and $2p_{3/2} \rightarrow (4f^0)5d$ transitions, with an absorption edge shift of ~5 eV to higher energy is observed.[26] Using the position of the first XANES feature provides a convenient measure of oxidation state and with reference materials a calibration can be produced. The XANES shows that the Ce-TiO_2 materials all contain mixtures of Ce^{3+} and Ce^{4+}, Figure 6;

however, the as-made materials predominantly contain Ce^{3+}, while the samples heated at 400 ^{o}C contain predominantly Ce^{4+}. For comparison, XANES spectra of samples made with 15% Ce are also included: these contain some CeO_2 seen by powder XRD and the spectra show how the 'white line' characteristic of Ce^{3+} is relatively reduced in intensity in these materials. *In situ* XANES was used to investigate this further with spectra as a function of temperature. Figure 7 shows the oxidation states of cerium determined during this process: this clearly proves that any heat treatment at the temperatures typically used by others in calcination (above 300 ^{o}C) causes oxidation of Ce^{3+} to predominantly Ce^{4+} (average oxidation state >3.5). It is also apparent that the presence of lactic acid in the synthesis provides a means of maximising and stabilising the Ce(III) in the higher Ce-containing samples in their as-made form before heating: for example, compare Figure 7h with Figure 7d. All of the materials prepared in lactic acid contain mostly Ce^{3+} prior to calcination.

To summarise the structural studies, the Ce-TiO_2 prepared by solvothermal synthesis has the bulk anatase structure with lattice parameters that evolve with Ce content, which although may also be a particle size dependence, suggests that at least some of the Ce is incorporated into the anatase structure. The Ce is well distributed in the materials, shown by EELS mapping, and XANES shows the as-made materials include significant amount of Ce^{3+}. The inclusion of lactic acid in the materials appears to stabilise the Ce^{3+} and also results in a more defective structure, as seen by Raman spectroscopy. On heating in air much of the Ce^{3+} is oxidised to Ce^{4+}. Some residual organic is present in all samples, which may be surface bound given the small particle size deduced from diffraction and from TEM.

2. Photocatalytic Properties

Photocatalytic water reduction and oxidation experiments were used to examine the activity of the materials towards hydrogen and oxygen evolution. We have thus used conditions comparable to those used in others' work on titania photocatalysts, to allow direct comparison with previous literature, and we have used pure anatase TiO_2 to provide a reference material. We selected the

materials prepared in the presence of lactic acid for this study since they show the highest surface areas and the most locally disordered and locally defective structures. The results are summarised in Table 2. First we note that we observe only negligible oxygen production in the presence of our materials, in accordance to most reports in the literature on photocatalysis by titania materials.[2] For our materials hydrogen evolution does not occur under visible light and the data reported in Table 2 were measured under UV irradiation in the presence of sacrificial methanol and Pt catalyst. Reduction of water to yield hydrogen occurs readily under these conditions, however, with optimum hydrogen product rates approaching that of the 'black TiO_2' reported in the literature,[9] shown graphically in Figure 8, are found for the 0.5 mol% cerium sample in its as-prepared form. The activity drops away with increased Ce content, and addition of 5 mol % Ce gives lower activity than even pure anatase. Calcination of the samples in air at 400 °C causes dramatic loss of photocatalytic hydrogen reduction, with complete loss of activity for the 10% Ce samples and loss of ~40 % for the 0.5% Ce sample, and for samples prepared under anaerobic conditions (by purging synthesis solutions with nitrogen gas) the activity is also somewhat lower. Normalisation of the activity to the BET surface area, Figure 8, shows that the highest activity is seen for the material with the lowest Ce content. It is well known that the photocatalytic activity of TiO_2 depends on the polymorph, the crystallinity and the surface area,[27], but even considering these effects, our results suggest that the photocatalytic activity towards hydrogen generation can be further increased by inclusion of Ce^{3+} instead of Ce^{4+}. Furthermore, the conditions under which the materials were prepared shows that the balance of Ce oxidation states are the key in optimising activity.

In proposing a model for the high hydrogen evolution activity of the Ce-TiO_2 at low levels of Ce content we note that the characterisation data points towards the polycrystalline materials possessing significant amounts of Ce^{3+}. Measurement of UV-vis diffuse reflectance spectra allow the band gaps of the materials to be estimated (Figure 9 and Supporting Information): thus for a low Ce-content material in its as-made form a band-gap corresponding to ~2 eV is found, rather much smaller than for anatase TiO_2 (3.2 eV), whereas after calcination it is increased to ~2.5 eV.

It is relevant at this point to note that the *thermochemical* reduction of water by non-stoichiometric ceria has proved possible:[28] here the CeO_2 is rendered oxide-deficient by the high temperature (>800 °C) of the process, or by the introduction of trivalent dopant metal cations,[29] and the effect is to introduce Ce^{3+}. Most previous work on cerium doping in TiO_2 have, however, used calcination or annealing to crystallise materials at temperatures at or above 400 ºC, [15, 16, 17-19, 30] under which conditions it is obvious from our *in situ* XANES results that the majority of cerium is oxidised to the +4 oxidation state. Interestingly Liu *et al.* prepared Ce-doped titanate nanosheets by hydrothermal synthesis and found a mixture of Ce^{3+} and Ce^{4+}, and proposed that certain levels of cerium doping could significantly inhibit the combination of electron–hole pairs, thus improving photocatalytic properties.[31] Li *et al.* also found enhanced photocatalytic activity of Ce-TiO_2 towards degradation of a heterocyclic organo-sulfur molecule, which they ascribed to the presence of Ce^{3+}, although their material was prepared by sol-gel followed by annealing at 500 °C, so the catalysts probably contained rather less Ce^{3+} than in our materials.[19] Furthermore Luo *et al.* found that for mixed CeO_x-TiO_2 oxides prepared by wet impregnation of TiO_2 with nanocrystalline cerium oxide, materials with low Ce loading (1 wt%) that contained the largest proportion of Ce^{3+} gave the highest photocatalytic hydrogen production when normalised for surface area.[20]

Combining our findings with the band structures reported in the literature from Ce-doped TiO_2 we can propose a simple model for photocatalysis, as shown schematically in Figure 10. The presence of Ce^{4+} doping brings about a smaller band gap than TiO_2 by inserting an empty cerium 4f level beneath the Ti 3d levels. However, the cerium 4f level is so close to the minimum requirement of proton reduction potential that H_2 cannot be produced under visible light, which is the possible reason that there are reported Ce^{4+}-TiO_2 materials for organic decomposition rather than for water reduction.[16, 19] Under UV excitation, Ce^{4+}-doped TiO_2 shows activity of H_2 evolution but much lower than pure TiO_2, which is because that the excited electrons in Ti3d transfer to Ce4f due to a small energy gap, thus lowering the reduction activity. On the other hand, apart from UV absorption due to excitation from O2p to Ti3d, a visible absorption extending to very long wavelength is

observed on the Ce^{3+}-doped TiO_2, which may be due to absorption due to defects generated when doping cerium ions to TiO_2 crystal structure. As our experiments show, the visible absorption does not directly contribute to H_2 evolution as observed under visible irradiation. Under UV excitation, the generated holes can migrate to Ce 4f level thus reducing intrinsic charge recombination in TiO_2, which is the dominating factor in solar driven H_2 production from water.[32] The photoholes at the Ce4f level are positive enough to oxidise alcohol (the sacrificial hole scavenger), leaving longlived photoelectrons for proton reduction. Therefore Ce^{3+}-TiO_2 materials show a higher activity for H_2 production than pure TiO_2.

Experimental Section

Materials were prepared by solvothermal reactions between 0.5 M of titanium(IV) isopropoxide (Acros Organics) and 0.5 M cerium nitrate hexahydrate (Sigma-Aldrich, 99%) solutions in ethanol (Sigma-Aldrich, absolute). Appropriate amounts of the two solutions, to give the desired Ti:Ce ratio, were mixed to give a total volume of 50 mL. 1 mL lactic acid (Sigma-Aldrich) was added to some of the reactions at this point, and the whole solution was stirred for 1 hour before being sealed in a 125 mL Teflon-lined steel autoclave and heated in an oven pre-heated at 240 °C for 24 hours. The pale yellow solids were recovered by suction filtration and dried in air at 70 °C before further study. The samples are labelled n%Ce-TiO_2, to denote the molar percentage of Ce included in the samples.

Powder X-ray diffraction patterns were recorded at room temperature using a Panalytical X'Pert Pro MPD operating with monochromatic Cu $K\alpha_1$ radiation and equipped with a PIXcel solid-state detector. Full pattern analysis of powder patterns was performed using the Pawley method within the TOPAS software to determine lattice parameters.[33]

X-ray absorption fine structure spectra at the Ce L_{III}-edge were obtained from experiments at the beamline B18[34] of the Diamond Light Source, UK. This beamline provides

X-ray energies in the range 2.05–35 keV using a fixed-exit, double-crystal Si (111) monochromator, which provides an energy resolution ($\Delta E/E$) of 2×10^{-4}. All samples containing cerium were measured at room temperature and at 100, 200, 300, 400 and 500 ^{o}C under a static air atmosphere. A tube furnace was used for in situ XANES measurements in which powdered samples were heated in air: a region of 1.5 cm length in a 0.5 mm diameter quartz tube was filled with the sample and tightly plugged either end with glass wool to prevent the sample moving and held in a horizontal furnace with a low flow of air passed through the sample. The spectra were measured with a step size equivalent to less than 0.5 eV, and in each temperature 5 or 10 scans were collected depending on cerium concentration. CeO_2, $CeCl_3 \cdot 7H_2O$ and an equimolar mixture CeO_2-$CeCl_3 \cdot 7H_2O$ were used as well-defined cerium +4 +3 and +3.5 standards, respectively. Data were normalised using the program Athena[35] with a linear pre-edge and polynomial post-edge background subtracted from the raw $\ln(I_t/I_0)$ data.

The thermal behaviour of the powders was investigated by thermogravimetry (TGA) using a Mettler Toledo TGA/DSC 1-600 instrument under air with a heating rate of 10 ^{o}C min^{-1} from room temperature up to 1000 ^{o}C. Raman spectra were collected at room temperature using a Renishaw InVia Raman microscope equipped with an Ar^+ laser operating at 514.5 nm and Renishaw CCD laser. Infrared spectroscopy of materials was performed with direct measure of the powder samples using a Perkin Elmer Paragon 1000 FTIR Spectrometer coupled with ATR apparatus. The specific surface areas of the samples were calculated by the BET method based on the N_2 adsorption isotherm data using a Micromeritics ASAP 2020 analyser. The samples were degassed at 200 °C for 10 h under vacuum to remove surface contamination and adsorbed species. A Shimadzu 2550 UV-Vis spectrometer equipped with an integrating sphere was used to record the absorption of powder samples, using barium sulphate powder as a reference. The reflection measurement was converted to an absorption spectrum using the Kubelka-Mulk transformation.

Scanning transmission electron microscopy (STEM) was performed using a JEOL ARM200F double aberration corrected instrument operating at 200 kV. Specimens were dispersed

by ultrasound in ethanol and dropped onto 3 mm lacey carbon grids supplied by Agar. High angle annular dark field (HAADF) images were produced and EELS spectrum imaging (EELS-SI) studies were performed on the instrument with a Gatan GIF Quantum ER spectrometer. For EELS-SI a dispersion of 0.5 eV/channel was set and spectra with 2048 channels were recorded with an energy range of 1024 eV in each spectrum. Gatan spectrum imaging plugin was used for EELS-SI acquisitions and elemental maps of Ti $L_{2,3}$-edge and Ce $M_{4,5}$-edge were produced after a suitable pre-edge inverse power law background fitting with energy windows of 30 eV and 45 eV, respectively (see Supporting Information for a typical individual EELS spectrum). This yields a 3D data set with each pixel containing an individual EELS spectrum

Reduction reactions (protons to H_2) were used to analyse the photoactivity of the materials. All reactions were carried out in a custom Pyrex® batch reactor cell (3.6 cm diameter of reactor window), which was thoroughly purged with argon prior to radiation. Gas concentration analysis was performed using a GC (Varian 430-GC, TCD, argon carrier gas 99.999%). For a typical reduction reaction, the photocatalyst (0.05g) was suspended and subsequently sonicated in a deionised water/hole scavenger mixture (230 mL total volume; 200 mL DI water, 60 mL methanol hole scavenger). Pt (acting as a co-catalyst) was then deposited onto TiO_2 using an *in situ* photodeposition method. Stock solutions of deionised water and precursors (*e.g.* Pt: $H_2PtCl_6 \cdot (H_2O)_6$) were made beforehand, and a set volume added according to the required weight of metal (1 wt%). The reactor was sealed, purged with Ar gas for 1 hour, and then irradiated for 1 hour under full arc irradiation using a 300 W Xe lamp (TrusTech PLS- SXE 300/300UV). During a one hour period, periodic measurements were taken to determine if hydrogen was being produced at a stable rate, and thus, if photodeposition had occurred correctly. The reactor was then purged a second time, prior to full arc irradiation. For oxygen production, no Pt was photodeposited, simply 0.25g of $AgNO_3$ was used as an electron scavenger, added to 230 ml deionised water. The reactor was sealed and purged with argon. As a reference, a sample of highly crystalline TiO_2 (pure anatase by powder XRD) was also studied using the same methodology.

Conclusions

A simple solvothermal synthesis method provides high activity photocatalysts based on polycrystalline titania in which the presence of Ce^{3+} is needed for optimal properties. In the literature most cerium-doped oxide nanomaterials have typically been prepared using an annealing step, for example, using sol gel chemistry followed by heating at >400 °C, where our XANES results show that oxidation of most cerium to the +4 oxidation state must occur. A key result from our work is that solvothermal synthesis allows the direct crystallisation of Ce^{3+}-rich titania materials. We thus demonstrate how the control of cerium oxidation state is clearly crucial for photocatalytic applications, allowing hydrogen production from water in the presence of sacrificial methanol and Pt catalyst. Further work is needed to establish the structural location of cerium and the local structure of these materials and this may include pair distribution analysis, requiring the acquisition of scattering data with high momentum transfer.

Acknowledgements

We thank the University of Warwick Brazil Partnership Fund, funded by Santander, and FAPESP (2013/11948-5 and 2012/24165-6) for providing grants for the visits of JFL to Warwick and RIW to Ribeirão Preto. PDW is grateful to the Leverhulme Trust (F/00215/AX) for funding and MHH thanks the Ministry of Education Brunei for award of a scholarship. Some of the equipment used in materials characterisation at the University of Warwick was obtained through the Science City Advanced Materials project "Creating and Characterising Next Generation Advanced Materials" with support from Advantage West Midlands (AWM) and part funded by the European Regional Development Fund (ERDF), and we thank Luke Daniels and Dr Ben Douglas for their help with using some of this equipment. We are grateful to Diamond Light Source for provision of beamtime for XANES measurements.

References

1. K. Hashimoto, H. Irie and A. Fujishima, *Jpn. J. Appl. Phys.*, 2005, **44**, 8269; X. Chen and S. S. Mao, *Chem. Rev.*, 2007, **107**, 2891.
2. A. Fujishima, X. T. Zhang and D. A. Tryk, *Surf. Sci. Rep.*, 2008, **63**, 515.
3. M. Ni, M. K. H. Leung, D. Y. C. Leung and K. Sumathy, *Renew. Sust. Energ. Rev.*, 2007, **11**, 401.
4. R. Janisch, P. Gopal and N. A. Spaldin, *J. Phys.: Condens. Matter*, 2005, **17**, R657.
5. L. G. Devi and R. Kavitha, *Appl. Catal. B-Environ.*, 2013, **140**, 559.
6. Y. Tang, P. Wee, Y. Lai, X. Wang, D. Gong, P. D. Kanhere, T.-T. Lim, Z. Dong and Z. Chen, *J. Phys. Chem. C*, 2012, **116**, 2772; S. G. Kumar and K. S. R. K. Rao, *Nanoscale*, 2014, **6**, 11574.
7. D. Wang, P. Kanhere, M. Li, Q. Tay, Y. Tang, Y. Huang, T. C. Sum, N. Mathews, T. Sritharan and Z. Chen, *J. Phys. Chem. C*, 2013, **117**, 22894−22902.
8. D. O. Scanlon, C. W. Dunnill, J. Buckeridge, S. A. Shevlin, A. J. Logsdail, S. M. Woodley, C. R. A. Catlow, M. J. Powell, R. G. Palgrave, I. P. Parkin, G. W. Watson, T. W. Keal, P. Sherwood, A. Walsh and A. A. Sokol, *Nat. Mater.*, 2013, **12**, 798; Q. Tay, X. Liu, Y. Tang, Z. Jiang, T. C. Sum and Z. Chen, *J. Phys. Chem. C*, 2013, **117**, 14973.
9. X. Chen, L. Liu, P. Y. Yu and S. S. Mao, *Science*, 2011, **331**, 746.
10. X. Chen, L. Liu and F. Huang, *Chem. Soc. Rev.*, 2015, DOI: 10.1039/c4cs00330f.
11. Y. H. Hu, *Angew. Chem., Int. Ed.*, 2012, **51**, 12410.
12. A. Trovarelli, ed., *Catalysis by Ceria and Related Materials, 2nd Edition*, World Scientific 2013.
13. R. D. Shannon, *Acta Crystallogr.*, 1976, **A32**, 751.
14. A. W. Xu, Y. Gao and H. Q. Liu, *J. Catal.*, 2002, **207**, 151; K. Gu, B. Chen, X. Wang, J. Wang, J. Fang, J. Wu and X. Yang, *Ind. Eng. Chem. Res.*, 2014, **53**, 6249.
15. J. Fang, H. Bao, B. He, F. Wang, D. Si, Z. Jiang, Z. Pan, S. Wei and W. Huang, *J. Phys. Chem. C*, 2007, **111**, 19078.
16. J. M. Xie, D. L. Jiang, M. Chen, D. Li, J. J. Zhu, X. M. Lu and C. H. Yan, *Coll. Surf. A*, 2010, **372**, 107; N. Yan, Z. Zhu, J. Zhang, Z. Zhao and Q. Liu, *Mater. Res. Bull.*, 2012, **47**, 1869.
17. S. W. Chen, J. M. Lee, K. T. Lu, C. W. Pao, J. F. Lee, T. S. Chan and J. M. Chen, *Appl. Phys. Lett.*, 2010, **97**, 012104
18. C. Gionco, M. C. Paganini, S. Agnoli, A. E. Reeder and E. Giamello, *J. Mater. Chem. A*, 2013, **1**, 10918.
19. F. B. Li, X. Z. Li, M. F. Hou, K. W. Cheah and W. C. H. Choy, *Appl. Catal. A - Gen.*, 2005, **285**, 181.
20. S. Luo, T.-D. Nguyen-Phan, A. C. Johnston-Peck, L. Barrio, S. Sallis, D. A. Arena, S. Kundu, W. Xu, L. F. J. Piper, E. A. Stach, D. Polyanskiy, E. Fujita, J. A. Rodriguez and S. D. Senanayake, *J. Phys. Chem. C*, 2015, **119**, 2669.
21. J. K. Burdett, T. Hughbanks, G. J. Miller, J. W. Richardson and J. V. Smith, *J. Am. Chem. Soc.*, 1987, **109**, 3639

22. M. I. Ahmad and S. S. Bhattacharya, *Appl. Phys. Lett.*, 2009, **95**; J. Kehres, J. W. Andreasen, F. C. Krebs, A. M. Molenbroek, I. Chorkendorff and T. Vegge, *J. Appl. Crystallogr.*, 2010, **43**, 1400; Z. Matej, L. Matejova and R. Kuzel, *Powder Diffr.*, 2013, **28**, S161; J. R. Eltzholtz, C. Tyrsted, K. M. O. Jensen, M. Bremholm, M. Christensen, J. Becker-Christensen and B. B. Iversen, *Nanoscale*, 2013, **5**, 2372.
23. T. Ohsaka, *J. Phys. Soc. Jpn.*, 1980, **48**, 1661.
24. H. C. Choi, Y. M. Jung and S. B. Kim, *Vib. Spectrosc*, 2005, **37**, 33.
25. B. Choudhury, B. Borah and A. Choudhury, *Mater. Sci. Eng. B-Adv. Funct. Solid-State Mater.*, 2013, **178**, 239.
26. S. Skanthakumar and L. Soderholm, *Physical Review B*, 1996, **53**, 920; Y. Takahashi, H. Sakami and M. Nomura, *Anal. Chim. Acta*, 2002, **468**, 345; P. W. Dunne, A. M. Carnerup, A. Wegrzyn, S. Witkowski and R. I. Walton, *J. Phys. Chem. C*, 2012, **116**, 13435.
27. A. Kudo and Y. Miseki, *Chem. Soc. Rev.*, 2009, **38**, 253.
28. W. C. Chueh, C. Falter, M. Abbott, D. Scipio, P. Furler, S. M. Haile and A. Steinfeld, *Science*, 2010, **330**, 1797.
29. A. Le Gal and S. Abanades, *J. Phys. Chem. C*, 2012, **116**, 13516; J. R. Scheffe, R. Jacot, G. R. Patzke and A. Steinfeld, *J. Phys. Chem. C*, 2013, **117**, 24104.
30. T. Tong, J. Zhang, B. Tian, F. Chen, D. He and M. Anpo, *J. Colloid Interface Sci.*, 2007, **315**, 382; A. M. T. Silva, C. G. Silva, G. Drazic and J. L. Faria, *Catal. Today*, 2009, **144**, 13; G. Xiao, X. Huang, X. Liao and B. Shi, *J. Phys. Chem. C*, 2013, **117**, 9739; S. Kityakarn, A. Worayingyong, A. Suramitr and M. F. Smith, *Mater. Chem. Phys.*, 2013, **139**, 543.
31. Y. Liu, P. Fang, Y. Cheng, Y. Gao, F. Chen, Z. Liu and Y. Dai, *Chem. Eng. J.*, 2013, **219**, 478.
32. J. Tang, A. J. Cowan, J. R. Durrant and D. R. Klug, *J. Phys. Chem. C*, 2011, **115**, 3143; J. Tang, J. R. Durrant and D. R. Klug, *J. Am. Chem. Soc.*, 2008, **130**, 13885.
33. A. Coelho, *TOPAS-Academic V5, Coelho Software* 2012.
34. A. J. Dent, G. Cibin, S. Ramos, A. D. Smith, S. M. Scott, L. Varandas, M. R. Pearson, N. A. Krumpa, C. P. Jones and P. E. Robbins, *14th International Conference on X-Ray Absorption Fine Structure (XAFS14), Proceedings*, 2009, **190**, 4.
35. B. Ravel and M. Newville, *J Synchrotron Radiat*, 2005, **12**, 537.

Table 1: Crystal Size from Scherer analysis of powder XRD data and BET surface areas for samples prepared in the presence and absence of lactic acid.

Sample	Surface Area / $m^2 g^{-1}$ No Lactic Acid	Crystal Size / nm No Lactic Acid	Surface Area / $m^2 g^{-1}$ Lactic Acid	Crystal Size / nm Lactic Acid
0.5% Ce-TiO_2	105.4	9.5	193.7	8.2
1%Ce-TiO_2	147.0	11.6	187.5	8.4
5%Ce-TiO_2	99.0	34.6	169.9	10.0
10%Ce-TiO_2	134.3	35.4	136.1	15.7

Table 2: Photocatalytic activity for hydrogen production (UV + visible radiation).

Sample	H_2 / μmol h^{-1} g^{-1}	O_2 / μmol h^{-1} g^{-1}
TiO_2 (anatase)[a]	1331	56
0.5%Ce- TiO_2	4972	28
0.5%Ce- TiO_2 (N_2)[b]	2214	40
1%Ce- TiO_2	2155	Not detected
5%Ce- TiO_2	657	Not detected
10%Ce- TiO_2	296	Not detected
10%Ce- TiO_2 (heated)[b]	185	Not detected
0.5%Ce- TiO_2 (heated)[b]	3033	Not detected

a: commercial sample of pure anatase; b:sample prepared after purging reaction solution with nitrogen; c: sample heated to 400 ^oC in air for 3 hours.

Figure captions:

Figure 1: Powder XRD of Ce-TiO2 materials prepared in the presence of lactic acid. The Miller indices are from the tetragonal unit cell expected for the anatase polymorph of TiO2 ($I4_1/amd$) and the lower sticks represent the relative peak intensities of the reference pattern for anatase.

Figure 2: Refined unit cell tetragonal parameters for Ce-TiO2 (a) a and (b) c, prepared in the presence and absence of lactic acid, along with the (c) unit cell volume. The dotted lines represent the lattice parameters expected for crystalline anatase (JCPDS 84-185).

Figure 3: Electron microscopy of selected Ce-TiO_2 samples (prepared with lactic acid): (a) HAADF-STEM of 1%Ce-TiO_2, (b) Ti element map using the Ti $L_{2,3}$-edge and (c) Ce element map using the Ce $M_{4,5}$-edge and (d) HAADF-STEM of 10%Ce-TiO_2, (e) Ti element map using the Ti L2,3-edge and (f) Ce element map using the Ce $M_{4,5}$-edge. In (a) and (d) the green marked regions are those used for element mapping.

Figure 4: Raman spectra of Ce-TiO_2 prepared (a) without lactic acid and (b) with lactic acid. The insets show the peak positions and widths of the $E_g(1)$ band, plotted on the same axes in (a) and (b) to emphasise the differences.

Figure 5: IR spectra of Ce-TiO_2 prepared (a) without lactic acid and (b) with lactic acid.

Figure 6: Ce L_{III}-edge XANES spectra of Ce-TiO_2 prepared (a) without lactic acid and (b) with lactic acid plotted with reference spectra of CeO_2 and $CeCl_3 \cdot 7H_2O$.

Figure 7: Average oxidation state of cerium in Ce-TiO_2 materials upon heating in air determined from in situ Ce L_{III}-edge XANES (a)-(d) materials prepared in the absence of lactic acid and (e)-(h) prepared using lactic acid. Lines are a guide for the eye.

Figure 8: Plot of the photocatalytic hydrogen evolution activity normalised to the surface area of the Ce-TiO_2 materials.

Figure 9: UV-Vis spectra of photocatalyst samples.

Figure 10: Model for the origin of photocatalytic activity of (b) Ce^{3+} -TiO_2 compared to (a) TiO_2 and also (c) Ce^{4+} -CeO_2 formed on annealing in air.

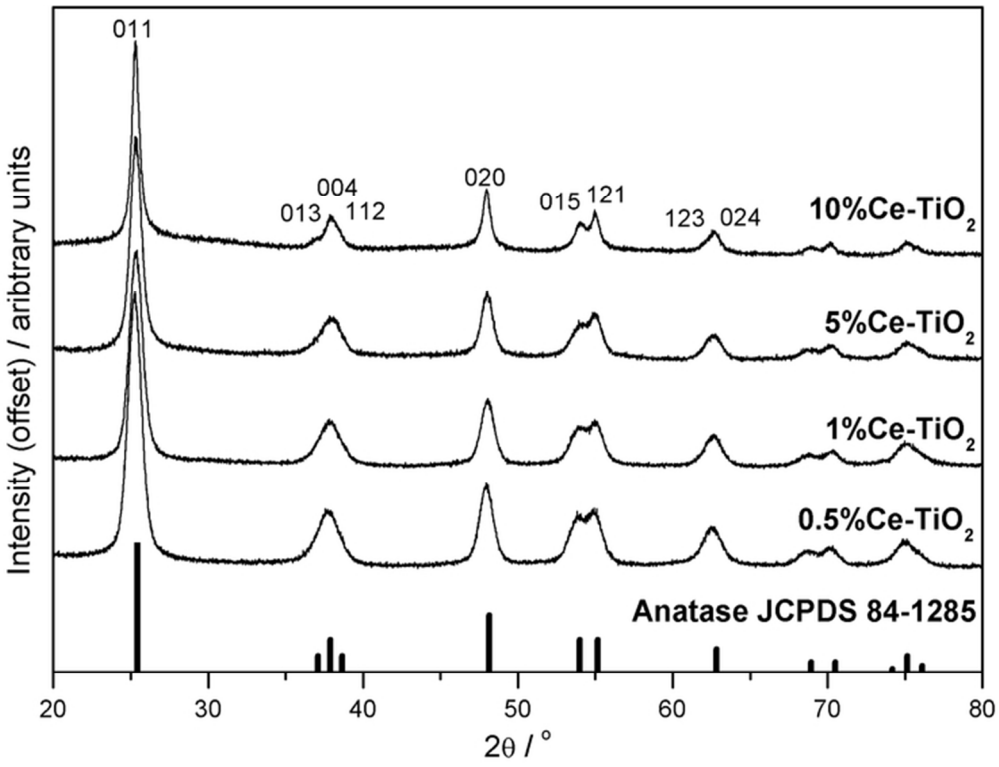

62x47mm (300 x 300 DPI)

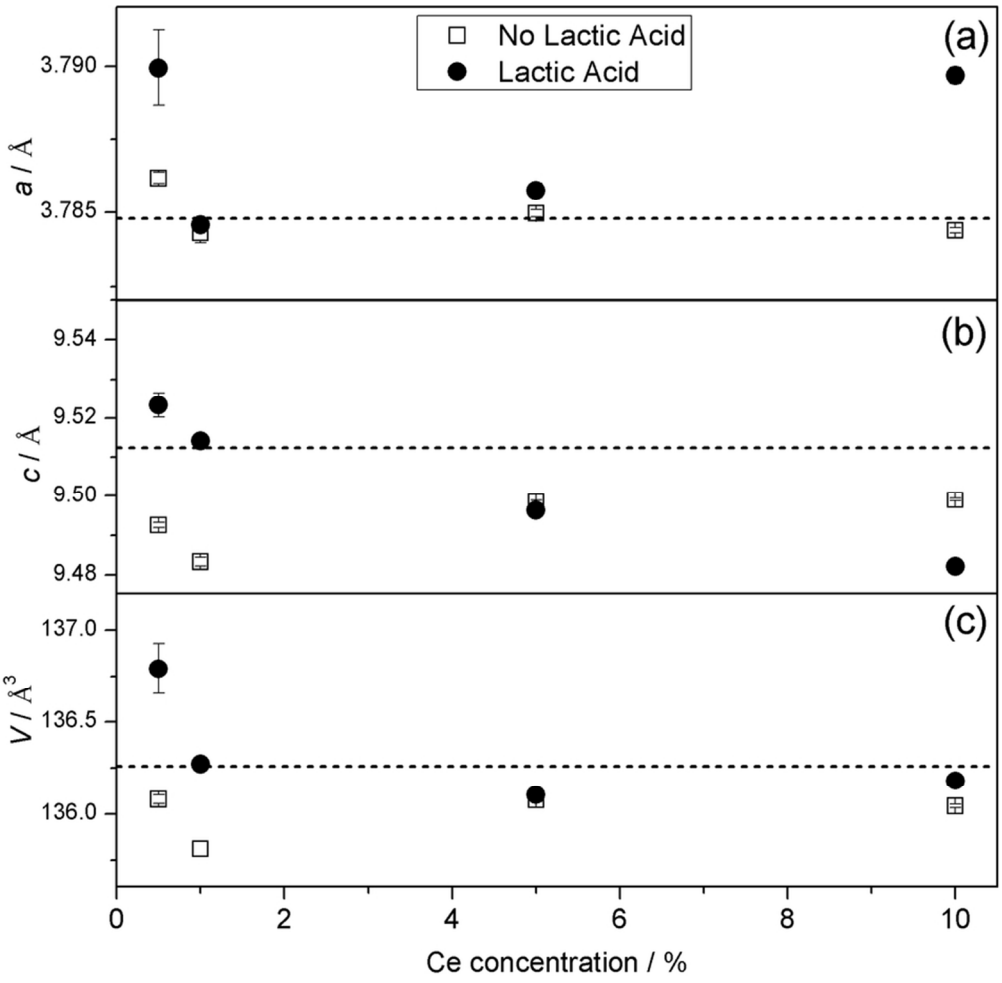

80x78mm (300 x 300 DPI)

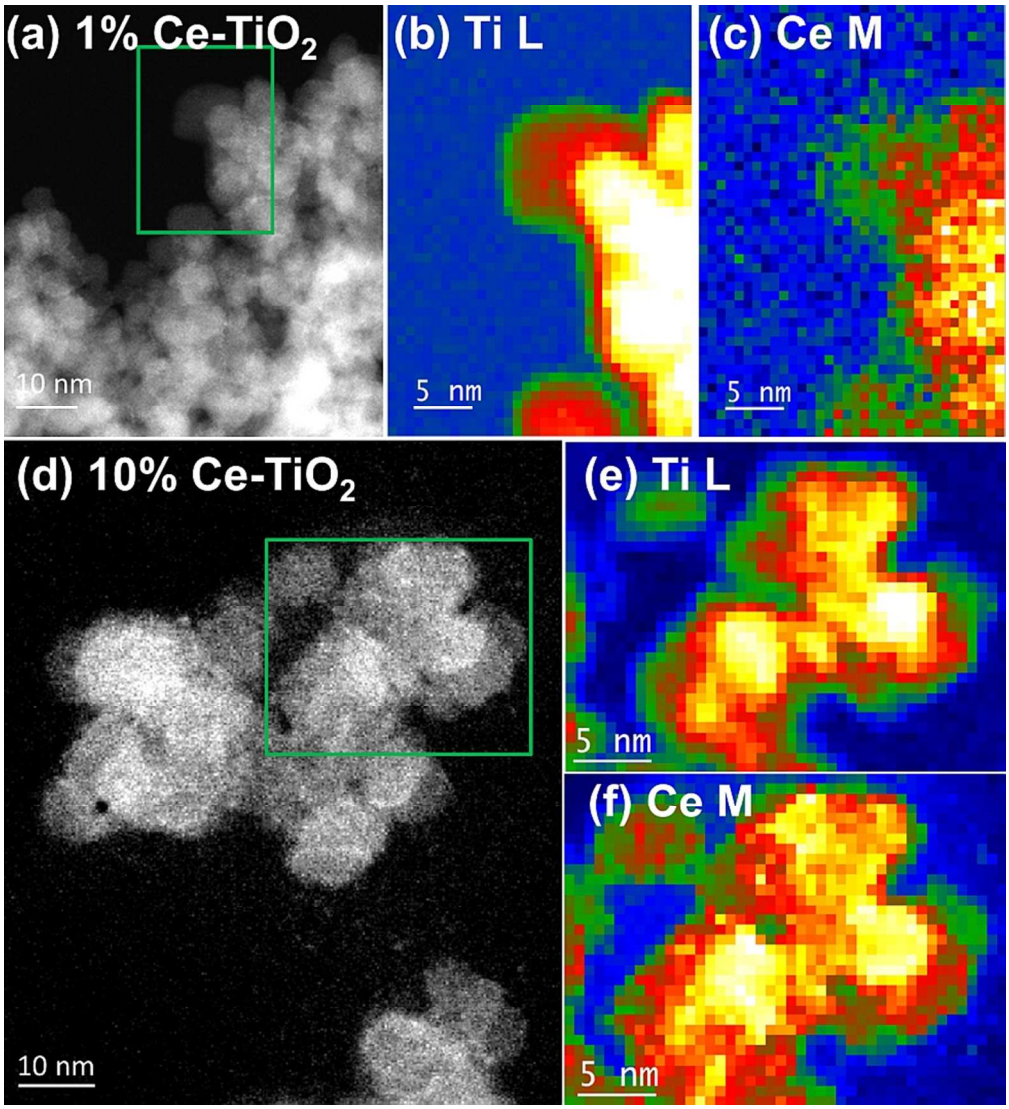

82x90mm (300 x 300 DPI)

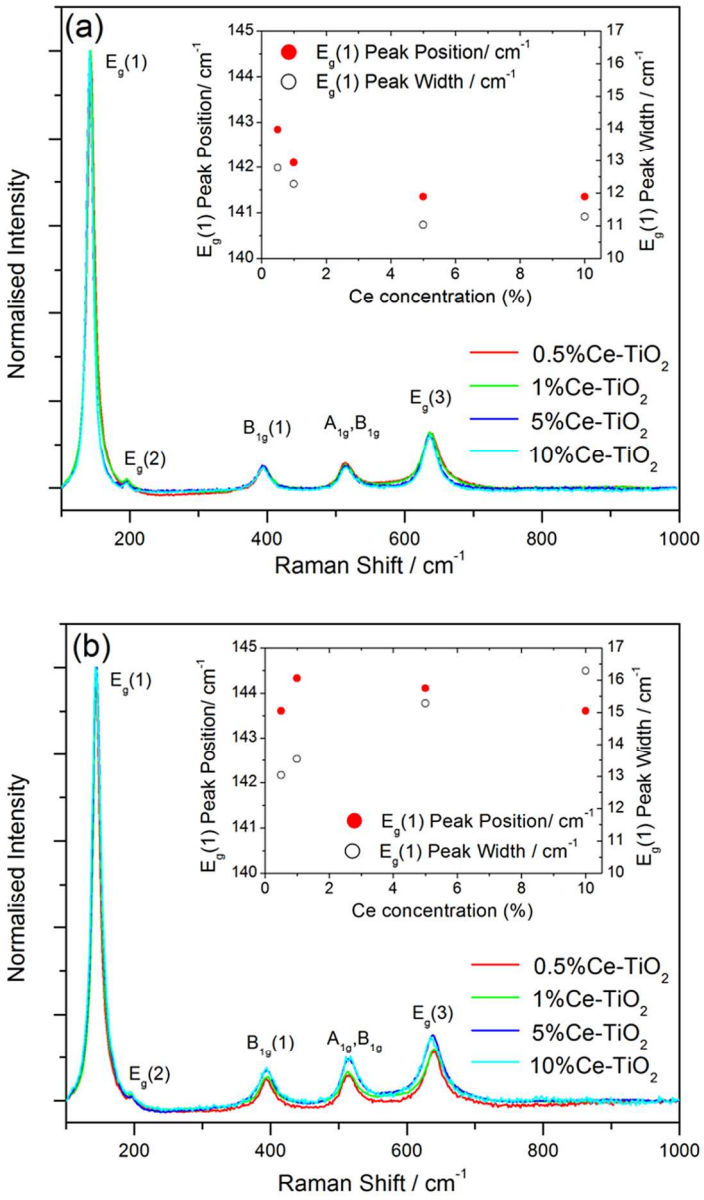

82x140mm (300 x 300 DPI)

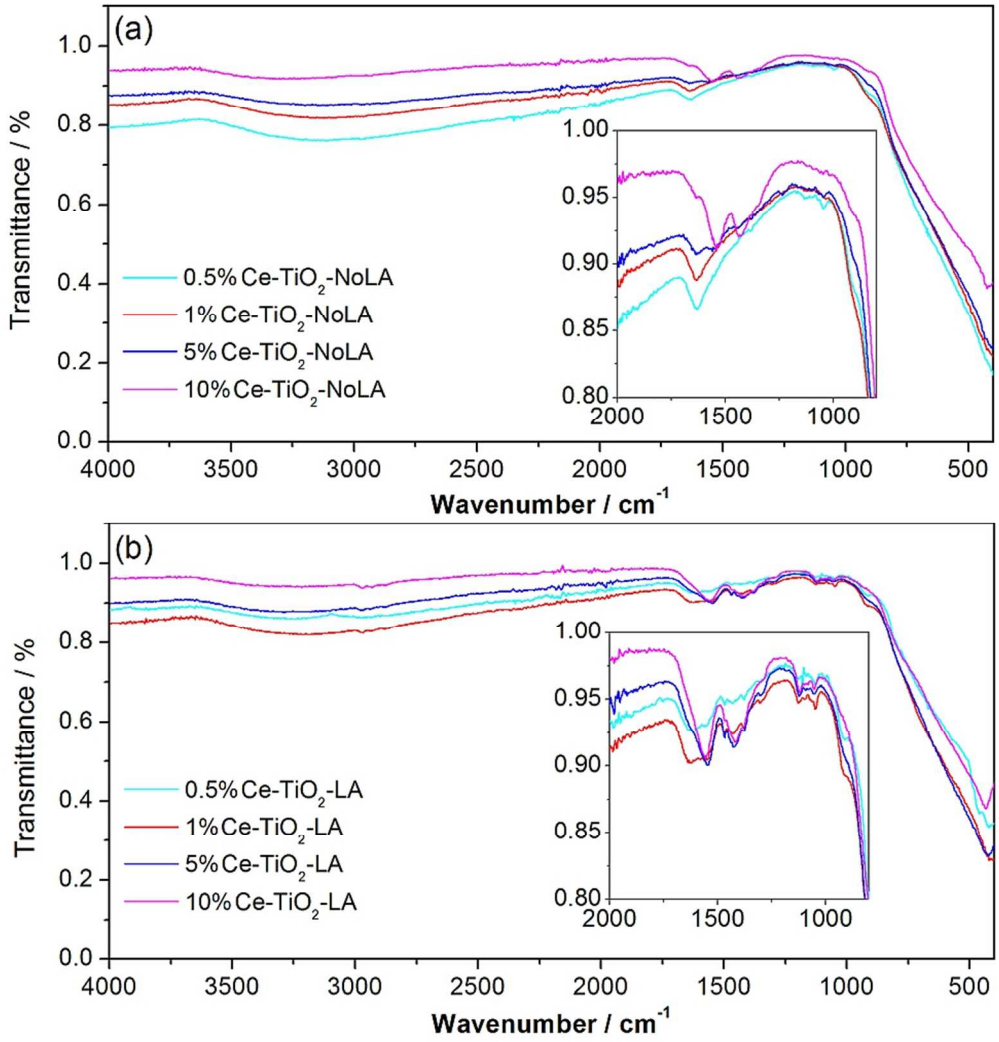

82x85mm (300 x 300 DPI)

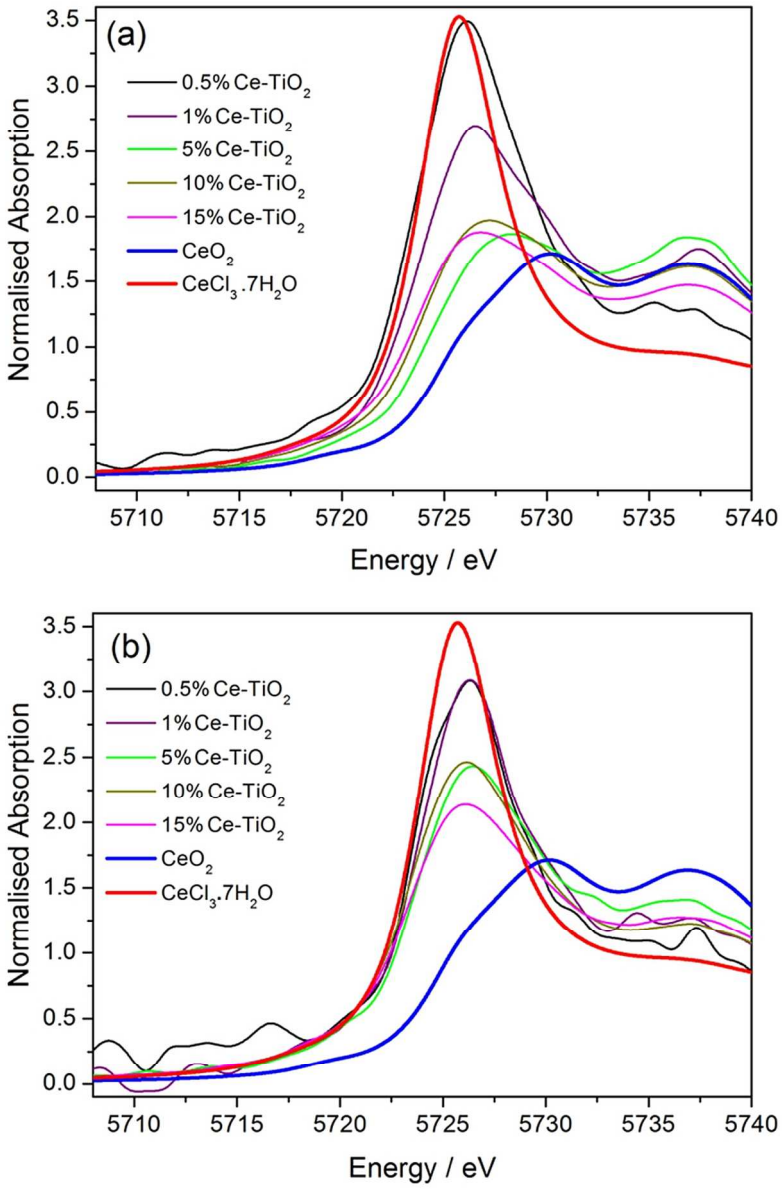

82x125mm (300 x 300 DPI)

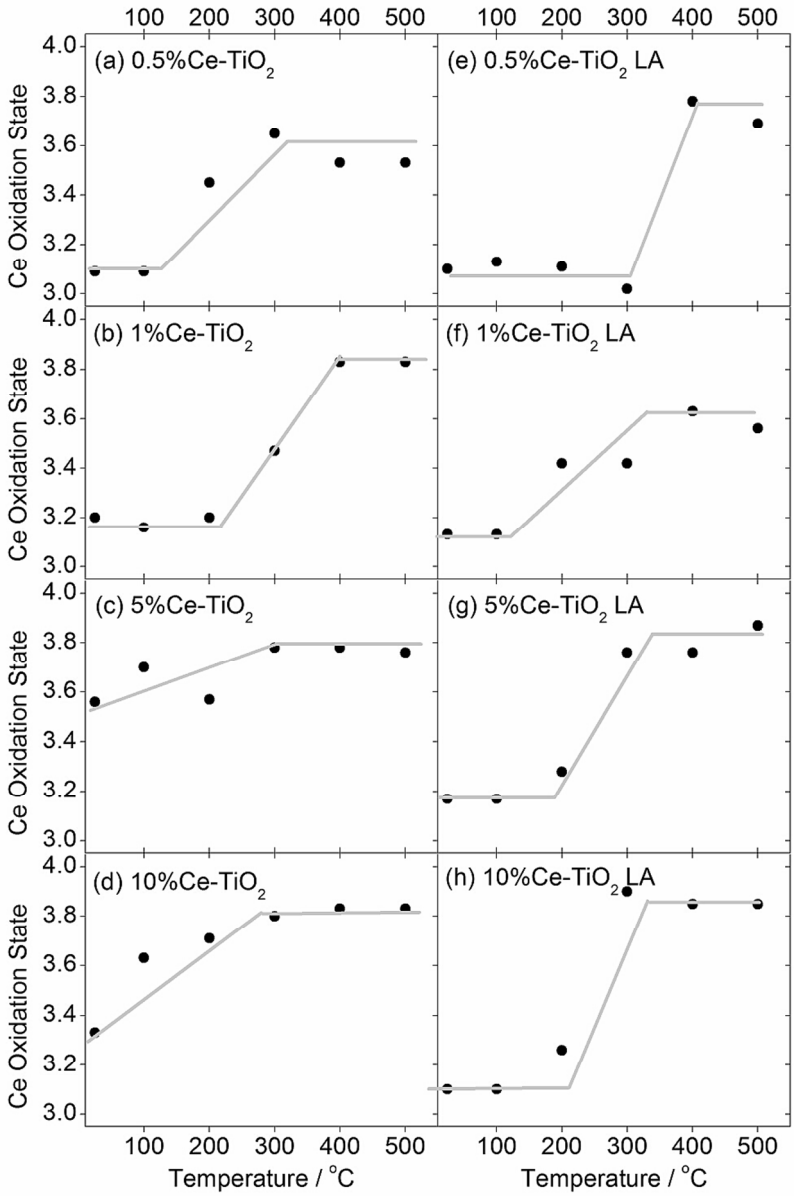

82x124mm (300 x 300 DPI)

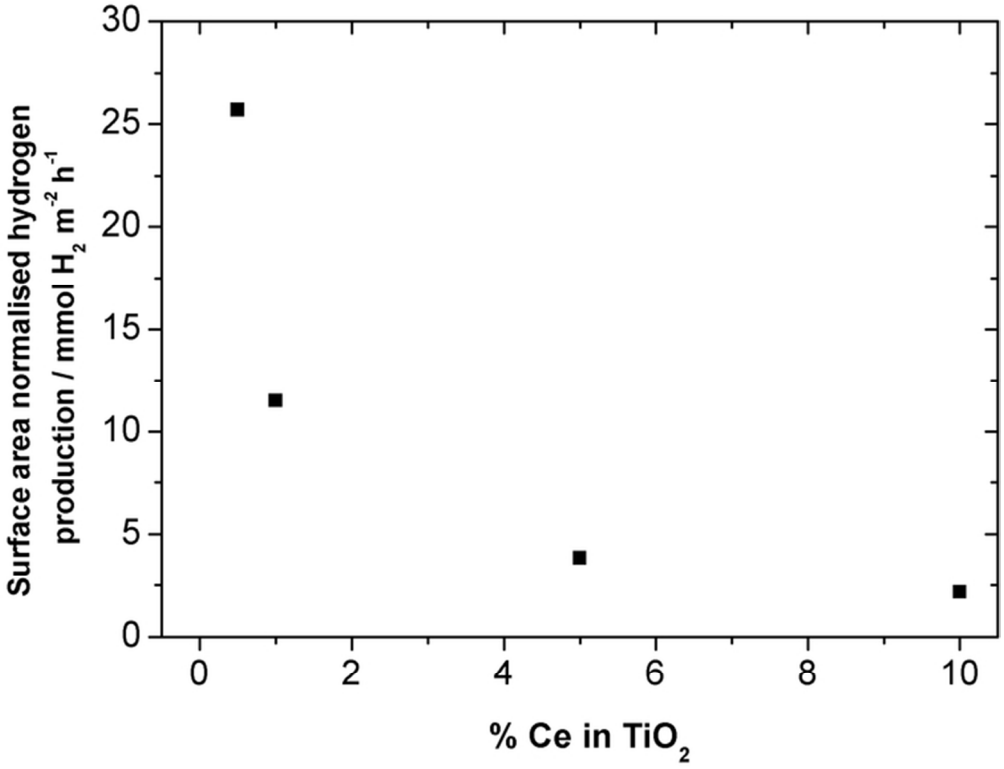

63x49mm (300 x 300 DPI)

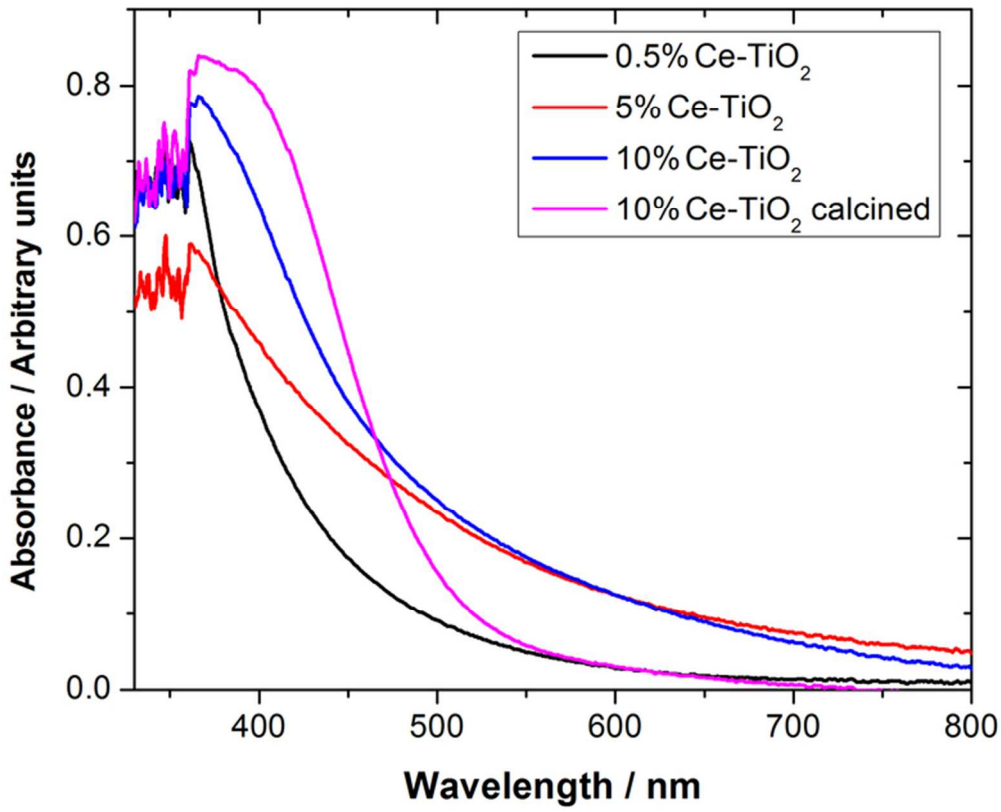

66x52mm (300 x 300 DPI)

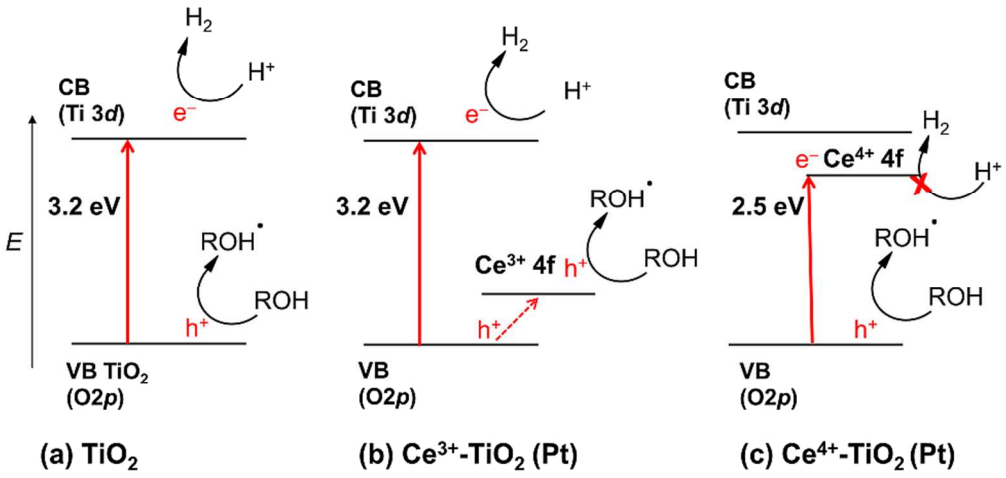

82x39mm (300 x 300 DPI)